



HAL
open science

Distribution of Pa in the Atlantic sector of the Southern Ocean: Tracking scavenging during water mass mixing along neutral density surfaces

M. Levier, M. Roy-Barman, L. Foliot, A. Dapoigny, F. Lacan

► To cite this version:

M. Levier, M. Roy-Barman, L. Foliot, A. Dapoigny, F. Lacan. Distribution of Pa in the Atlantic sector of the Southern Ocean: Tracking scavenging during water mass mixing along neutral density surfaces. *Deep Sea Research Part I: Oceanographic Research Papers*, 2023, 194, pp.103951. 10.1016/j.dsr.2022.103951 . hal-04044045

HAL Id: hal-04044045

<https://hal.science/hal-04044045>

Submitted on 27 Nov 2023

HAL is a multi-disciplinary open access archive for the deposit and dissemination of scientific research documents, whether they are published or not. The documents may come from teaching and research institutions in France or abroad, or from public or private research centers.

L'archive ouverte pluridisciplinaire **HAL**, est destinée au dépôt et à la diffusion de documents scientifiques de niveau recherche, publiés ou non, émanant des établissements d'enseignement et de recherche français ou étrangers, des laboratoires publics ou privés.

Distribution of Pa in the Atlantic Sector of the Southern Ocean: Tracking scavenging during water mass mixing along neutral density surfaces

M.Levier¹, M.Roy-Barman[†], L.Foliot¹, A.Dapoigny¹, F.Lacan²

1 Laboratoire des Sciences du Climat et de l'Environnement (LSCE), Gif-sur-Yvette, France

2 Laboratoire d'Etude de Géophysique et Océanographie Spatiale (LEGOS), Toulouse, France

Abstract :

Dissolved and particulate ²³¹Pa was analyzed for samples from the BONUS GoodHope (BGH) IPY-GEOTRACES cruise in the SE Atlantic sector of the Southern Ocean (36°S-13°E to 57°S-0°, Feb.–Mar. 2008). Inflowing water from the Atlantic Ocean fuel the Antarctic Circumpolar Current in dissolved ²³¹Pa which is mostly removed from seawater by the biogenic silica produced by diatoms in the Southern Ocean. This scavenging flux of the ²³¹Pa induces a meridional gradient of the ²³¹Pa concentration and of the Th-Pa fractionation factor ($F_{Th/Pa}$).

We propose a first direct estimate of the ²³¹Pa partition coefficient between suspended opal and seawater of about $2 \pm 0.5 \times 10^6$ g/g. We apply to ²³¹Pa the isopycnal advection-diffusion-scavenging model built for Th isotopes across the ACC. This additional constrain on the model does not modify the isopycnal eddy diffusion estimate of about 2000 ± 200 m²/s at different isopycnal surfaces but suggests a higher particle settling velocity, about 1000 m/y, in the northern part of the ACC than just with Th isotopes. The most different features is the reduction by half of the estimated uncertainties among the different transport parameters just by the addition of a new constraining parameter.

Keywords: Protactinium, Mass spectrometry, marine particles, Southern Ocean, isopycnal mixing

1. Introduction

Protactinium 231 (^{231}Pa) is a radioactive isotope produced at a constant rate in seawater by the decay of uranium 235 (^{235}U). Dissolved ^{231}Pa has a residence time in seawater of a few centuries controlled by scavenging by marine particles, so most of the ^{231}Pa produced *in situ* is transported toward the sediment.

^{230}Th is also a particle reactive isotope produced at constant rate in seawater by the decay of uranium 234 (^{234}U). The difference of particle reactivity of ^{231}Pa and ^{230}Th induces deviations of the $^{231}\text{Pa}/^{230}\text{Th}$ ratios of seawater, marine particles and sediments from the production activity ratio (0.093) (Rutgers van der Loeff and Berger, 1993). The Pa/Th ratio in sediments is used as a paleoproxy of the ventilation of deep water in the meridional circulation of the Atlantic Ocean. Along a meridional transect of the Atlantic Ocean, $^{231}\text{Pa}/^{230}\text{Th}$ ratio measured in seawater increases from north to south. South of the Atlantic Ocean, a change of the $^{231}\text{Pa}/^{230}\text{Th}$ ratio is observed due to the enhanced scavenging of ^{231}Pa by diatoms (Scholten et al., 2008). While the affinity of ^{231}Pa for biogenic opal is well recognized (Chase et al., 2002; DeMaster, 1981; Gdaniec et al., 2020; Geibert and Usbeck, 2004; Lin et al., 2014; Yu et al., 1996), there is no direct quantification of the affinity of ^{231}Pa for biogenic opal in suspended particles from the water column (Hayes et al., 2015) and on the impact of biogenic opal dissolution in deep waters on the ^{231}Pa particulate flux (Gdaniec et al., 2020).

^{231}Pa budget of the Atlantic sector of the Southern Ocean shows that the main source of ^{231}Pa to the Antarctic Circumpolar Current (ACC) is the inflow from the Atlantic Ocean, half of it being removed by scavenging in the Weddell gyre (Rutgers van der Loeff et al., 2016). The other half of the inflowing Pa is exported to the Pacific sector of the Southern Ocean where ^{231}Pa is also scavenged or exported to the Pacific Ocean through isopycnal mixing (Pavia et al., 2020). The removal of ^{231}Pa upwelling from the South Atlantic in the Weddell gyre results from a double trap : first by the gyre circulation preventing intermediate ^{231}Pa -rich waters to flow northward, enhancing the ^{231}Pa scavenging in the center of the gyre, and second by Pa scavenging in the opal belt (area of high diatom production, around 52°S), when Weddell Sea Deep Water (WSDW) flows out the gyre (Rutgers van der Loeff et al., 2016).

Here, we analyze dissolved and particulate ^{231}Pa in samples collected across the Antarctic Circumpolar Current (ACC) during the Bonus GoodHope cruise in the Southern sector the

Atlantic Ocean. The Bonus GoodHope section samples were previously analyzed for thorium isotopes (Roy-Barman et al., 2019).

Thorium isotopes transport across the ACC was described with an advection-diffusion-scavenging model along isopycnal surfaces, allowing to estimate isopycnal advection and eddy diffusion coefficients as well as particles settling velocity. We want to extend this model to protactinium isotopes to get further insight in the behavior of ^{231}Pa , notably to determine mixing rate of Pa across the ACC. By comparing ^{231}Pa and Si data, we want to constrain the processes controlling ^{231}Pa scavenging. Finally, ^{230}Th and ^{231}Pa data comparison will give insight in the fractionation of these elements by marine particles.

2. Methods

2.1. Hydrologic context

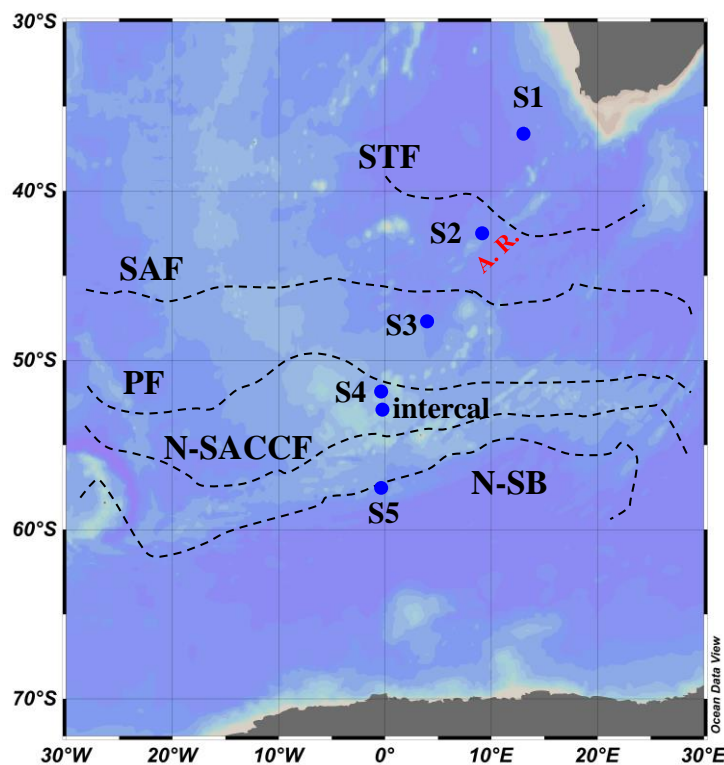


Figure 1 : Map of the stations from the Bonus GoodHope cruise, with the different front across the Southern Ocean

The main water masses and currents encounter during the Bonus GoodHope cruise were

described in details elsewhere (Abadie et al., 2017; Bown et al., 2011; Chever et al., 2010; Garcia-Solsona et al., 2014). The section is characterized by three main hydrological and circulation domains: the Subtropical domain (Station S1), the Antarctic Circumpolar Current (ACC; S2 to S4) and the Weddell Sea Gyre (S5). The subtropical domain is bounded to the south by the subtropical front (STF), which was located around 41°S-42°S, north of S2. The ACC domain includes the Subantarctic Front (SAF; ~45°S) and the Polar Front (PF; ~50°S) (Fig. 1). It is bounded to the south by the southern ACC boundary (Sby). From the Sby to the Antarctica, water circulation is dominated by the cyclonic Weddell Gyre (WG; S5) (Roy-Barman et al., 2019).

Water mass transport along the BGH section is mainly zonal. In the subtropical domain (station S1), it is dominated by the westward flowing Agulhas Current in the upper water column ($z < 1500$ m) and at depth by the eastward transport of SE-NADW (Sokolov and Rintoul, 2009). Stations S2, S3 and S4 are located within the Antarctic Circumpolar Current, flowing eastward throughout the water column. Finally, the Weddell gyre is a mainly wind-driven cyclonic gyre (Ryan et al., 2016), constrained by topographic boundaries except in the East, where mixing occurs between ACC and Weddell Gyre water masses (Gouretski and Danilov, 1993; Schröder and Fahrbach, 1999). The Circumpolar Deep Water (CDW) inflowing the Weddell Gyre, is called Warm Deep Water (WDW). It circulates from the East to the West in the southern part of the Weddell Gyre. The WDW is modified by upwelling into and mixing with shallower water and makes its way to the southern part of the Weddell Sea. By cooling and brine rejection during winter, the cold Weddell Sea Deep Water (WSDW) and Weddell Sea Bottom Water (WSBW) are formed (Nicholls et al., 2009) and flow northward, following the cyclonic gyre circulation. A significant fraction of the WSDW is exported to the North and mixes with the ACC at the Scotia Ridge. The remaining fraction flows toward the northeast of the Weddell Gyre, where the station S5 is located. This water partly recirculates in the gyre by mixing with the Circumpolar Deep Water incoming from east to form the new WDW (Deacon, 1979; Gouretski and Danilov, 1993).

The BGH section is approximately perpendicular to the mean flows of the ACC, so the BGH stations are not hydrologically connected and there might be no direct mixing between the stations. However, slower meridional transport were noted on meridional sections of water mass tracers such as salinity, temperature or iron isotopes, revealing notably the northward transport of AAIW and AABW, and southward transport of NADW (Abadie et al., 2017; Roy-Barman

et al., 2019). This meridional transport is assumed to be a residual flow from the Atlantic Ocean circulation in which lateral eddy fluxes largely balance the wind-driven circulation (Marshall and Speer, 2012). In the following, we apply a simple transport model of advection-diffusion-scavenging to link tracer properties measured along the BGH meridional section (Roy-Barman et al., 2019). The transports are not assumed to be a true meridional mixing along the BGH section, but it allows to estimate the residual meridional component of the mixing (advection, diffusion) embedded in the dominant zonal of the ACC Atlantic sector.

2.2. Sampling

The BONUS GoodHope cruise occurred from February 8th 2008 to March 17th 2008, during the late austral summer, on board Marion-Dufresne II Research Vessel. Samples were collected along a transect between 34°S 19°E and 51°S 0°W and then along the Greenwich meridian from 51°S to 58°S. Five full depth vertical profiles were sampled (S1-S5 stations) for both dissolved and particulate ^{231}Pa analysis. Three depths were collected for dissolved ^{231}Pa analysis at an intercalibration station. Seawater samples were collected with Niskin bottles mounted on a rosette, equipped with a CTD sensor. Challenger Oceanic in situ pumps (ISP) were used to filter large seawater volumes through SUPOR filters (pore size: 0.45 μm , filter diameter: 293 mm) seawater volumes filtered were ranging from 200 L to 1000 L.

2.3. Analytical procedure

2.3.1. Filtered seawater

Ten liters of filtered seawater (NucleporeTM, 90mm diameter, 0.4 μm pore size) were acidified at $\text{pH} = 2$ with HCl on board. The samples were processed in a clean lab for the simultaneous extraction of ^{227}Ac and ^{231}Pa as describe in Levier and al. (2021). To summarize, samples were spiked with ^{233}Pa , previously milked from ^{237}Np on hydrated silica (Guihou et al., 2010). Pa isotopes were preconcentrated using manganese oxides co-precipitation (Ghaleb et al., 2004; Rutgers van der Loeff and Moore, 1999). The precipitate was recovered on NucleoporeTM filter (diameter 142mm, 0.45 μm pore size). The precipitate still on the filter was dissolved in a bath of 6 M HCl with 100 μL of H_2O_2 and 100 μL of 27 M HF during 30min. The filter was then rinsed with 6M HCl. After evaporation of the dissolution bath, the residue was dissolved in 0.5 mL of 9 M HCl and loaded on an anion-exchange column (AG1-X8 resin,

200-400 mesh) to separate the protactinium fraction, eluted with 9M HCl + 0.26M HF, from the major elements, uranium, thorium and rare earth elements (REEs) and actinium (Levier et al., 2021).

2.3.2. Particulate samples

Protactinium from particulate samples was recovered and purified during same chemistry as the particulate thorium isotopes (Roy-Barman et al., 2019). Filters from the *in situ* pumps were cut into pieces using ceramic scissors. Several leaching steps were necessary to recover Th without attacking the filters. Filter pieces were first leached with 200 mL of 6N HCl and 1.5 mL of 24-25N HF in a 300 mL Teflon beaker for 2 days at 75°C. The filter pieces were removed from the leaching solution and rinsed with a MQ water squeeze bottle over the leaching beaker. The filter pieces were saved apart. The leaching and rinsing solutions were evaporated down to ~10 mL and transferred into a 30 mL Teflon beaker. Then, the filter pieces were leached a second time with 150 mL of 7N HNO₃ and 0.05 mL of 29N HF for 2 days at 75°C. The filter pieces were removed from the leaching solution and rinsed with MQ water that was again recovered into the leaching beaker. After evaporation to a few mL, this solution was added to the first leaching and rinsing solution. The 300 mL Teflon beaker was rinsed in warm diluted HNO₃ to remove any particle sticking on the beaker walls and the resulting solution was also added to the 30 mL beaker. The resulting solution was then spiked with ²³³Pa (and ²²⁹Th), dried and dissolved again in a solution with 4 mL of 14N HNO₃ and 1 mL of 12N HCl. After 1 night on a hot plate, the solution was dried and the residue was dissolved again in 10 ml of 1N HNO₃. Since the filters were not rinsed immediately after filtration with distilled water on board, it was preferable to remove the salt before the column chemistry. Therefore, 40µL of a Fe solution (60 mg/g) were added. After 1h-heating, Fe was precipitated by raising the pH to about 8 with NH₃. The Fe precipitate (that coprecipitates Th and Pa isotopes) was separated by centrifugation and rinsed several times. Finally, it was dissolved in 0.25 ml of 8N HNO₃, ready for loading on an anionic column. Pa and Th isotopes were separated from Fe by ion exchange chromatography on a small volume (0.5 ml) column of AG1X8 (200-400 mesh) resin (Gdaniec et al., 2018, adapted from Jeandel et al., 2011).

2.4. Mass spectrometry

Every analysis was performed on a Multiple Collection Inductively Coupled Plasma Mass Spectrometer (MC-ICPMS) Neptune^{plus} (Thermo-Fischer) mounted with a jet interface and an Aridus II desolvation system based on a protocol derived from Guihou et al., 2010. The acquisition conditions of Pa measurements are given in Gdaniec et al., 2018. The calibration of ²³³Pa spike solution was made against an in-house ²³¹Pa standard, used for intercalibration exercises (Gdaniec et al., 2019 ; Gdaniec et al., in prep). Particle samples from stations S1 and S2, spike calibration was lost during the chemical separation. This loss made impossible the precise correction for the chemical yield. To circumvent this problem, we noted that for station S3, S4 and S5, the chemical yield ranged from 20% to 100%, but for each series the highest yield ranged from 80% to 100%. Therefore, we attributed a chemical yield of 90% ± 10% to the samples of stations S1 and S2 with the highest count rate on ²³³Pa and deduced the concentration of the spike solution by using the sensitivity (count per second per ppt) measured on a ²³¹Pa-²³³U calibration solution. This procedure was checked on stations S3, S4 and S5, the concentrations deduced for all samples fall within ± 10% of concentrations deduced from the true spike concentration obtained by the spike calibration against the home standard.

²³¹Pa concentrations were corrected for ingrowth from ²³⁵U decay between the on-board sampling and the U-Pa chemical separation (Levier et al., 2021). All uncertainties were propagated through signal processing equation and correction equation, and each of them were expressed with a confidence interval of 95% (2 times standard error: 2σ_n).

3. Results

In order to consider exclusively ²³¹Pa concentration produced *in situ* by the ²³⁵U decay, the ²³¹Pa concentrations measured by mass spectrometry were corrected from the contribution brought by lithogenic material, where we used ²³²Th as a proxy. The excess of ²³¹Pa was expressed as follows:

$${}^{231}\text{Pa}_{xs} = {}^{231}\text{Pa}_m - {}^{232}\text{Th}_m \times \left(\frac{{}^{238}\text{U}}{{}^{232}\text{Th}} \right)_{litho} \times \left(\frac{M_{231}}{M_{232}} \right) \times \left(\frac{\lambda_{232} \times \lambda_{235}}{\lambda_{238} \times \lambda_{231}} \right) \times \left(\frac{{}^{235}\text{U}}{{}^{238}\text{U}} \right)_{nat} \quad (3.1)$$

Where ²³¹Pa_{xs} is the excess of ²³¹Pa corrected from the lithogenic contribution, ²³¹Pa_m and ²³²Th_m are the measured isotopes (Roy-Barman et al. 2019). λ₂₃₀, λ₂₃₁, λ₂₃₅ and λ₂₃₈ are the decay constant of ²³⁰Th, ²³¹Pa, ²³⁵U and ²³⁸U respectively. M₂₃₁ and M₂₃₀ are the molar masses

of the ^{231}Pa and ^{230}Th . $(^{235}\text{U}/^{238}\text{U})_{\text{nat}}$ is abundance ratio between natural uranium isotopes, here 1/137.818 mol/mol (Livermore et al., 2018, Condon et al., 2010). The mean crustal activity ratio $(^{238}\text{U}/^{232}\text{Th})_{\text{litho}} = 0.4 \pm 0.1$, estimated south of the Antarctic Polar Front (Rutgers van der Loeff and Berger, 1993; Venchiarutti et al., 2011).

Dissolved protactinium 231 corrected from the lithogenic contribution ($^{231}\text{Pa}_{\text{d-xs}}$) measured for the Bonus GoodHope cruise ranged from 0.19 ± 0.02 fg/kg in surface water to 3.45 ± 0.06 fg/kg (Table) in bottom water with a general increase of the concentration with depth (Figure 2). At the stations S1 to S3, we observe a similar profile with a linear increase from the surface to around 1500m. At Station S1, we see a maximum concentration of 3.34 ± 0.06 fg/kg at 3000m, in NADW, and decrease to 2.79 ± 0.06 fg/kg at 4000m in the AABW. At station S3, there is a sharp decrease of the concentration near depth, from 2.75 ± 0.05 fg/kg at 3000m to 1.67 ± 0.04 fg/kg in the bottom water. This decrease was already noted for dissolved REE (Garcia Solsona et al., 2014) and thorium isotopes (Roy-Barman et al., 2019), (possibly due to hydrothermal scavenging, or a rich deep nepheloid layer.)

The Bonus GoodHope cruise occurred 3 weeks after the ZeroDrake cruise, where the Greenwich meridian was also sampled across the ACC for $^{231}\text{Pa}/^{230}\text{Th}$ studies (Rutgers van der Loeff et al., 2016; Venchiarutti et al., 2011). Thorium isotopes were consistent between the two cruises (Roy-Barman et al., 2019). Consistent data are also obtained for $^{231}\text{Pa}_{\text{xs}}$, when we compare stations S2 to S4 with nearby ZeroDrake stations (Figure ES10). At these stations, the BGH concentrations tend to be on the low side of the Drake values. However, an intercalibration exercise between LSCE and AWI, on strictly identical samples, proved an agreement within a few percent for ^{231}Pa measured in deep arctic sample (Gdaniec et al in prep). By contrast, in the Weddell Gyre, the dissolved $^{231}\text{Pa}_{\text{xs}}$ was almost twice less concentrated at Station S5 compared to station 131 of the ZeroDrake cruise. There is about 150 km between these stations (0.00E, 57.5S for the BGH sampling point and 0.00E, 59.0S for the ZeroDrake one). Possible reasons for this discrepancy will be discussed in section 4.1.

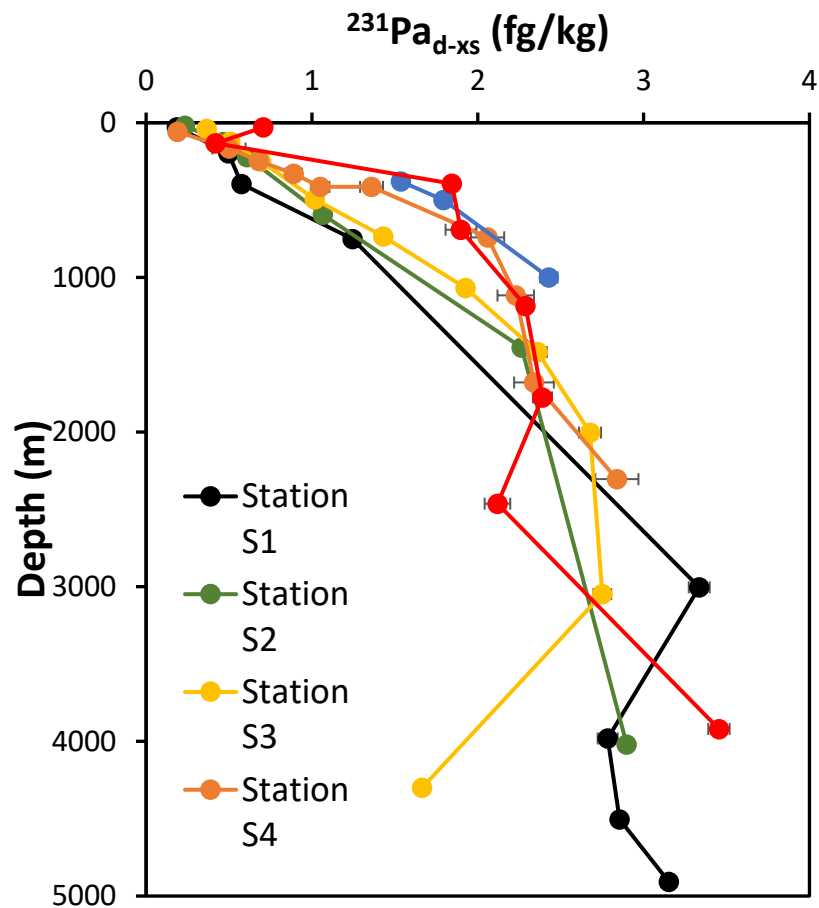


Figure 2 : $^{231}\text{Pa}_{\text{xs}}$ concentration in the dissolved phase of the super stations of the Bonus GoodHope cruise

The ^{231}Pa concentration in excess on the particulate fraction ($^{231}\text{Pa}_{\text{p-xs}}$) ranged from 0.00081 ± 0.00016 fg/kg in surface water (station S4) to 0.341 ± 0.054 fg/kg in bottom water of station S1 (Figure 3). The $^{231}\text{Pa}_{\text{p-xs}}$ concentration are rather constant through the water column with a sharp increase near the seafloor, except at station S3, where the deepest concentration remains similar to the intermediate waters (Table).

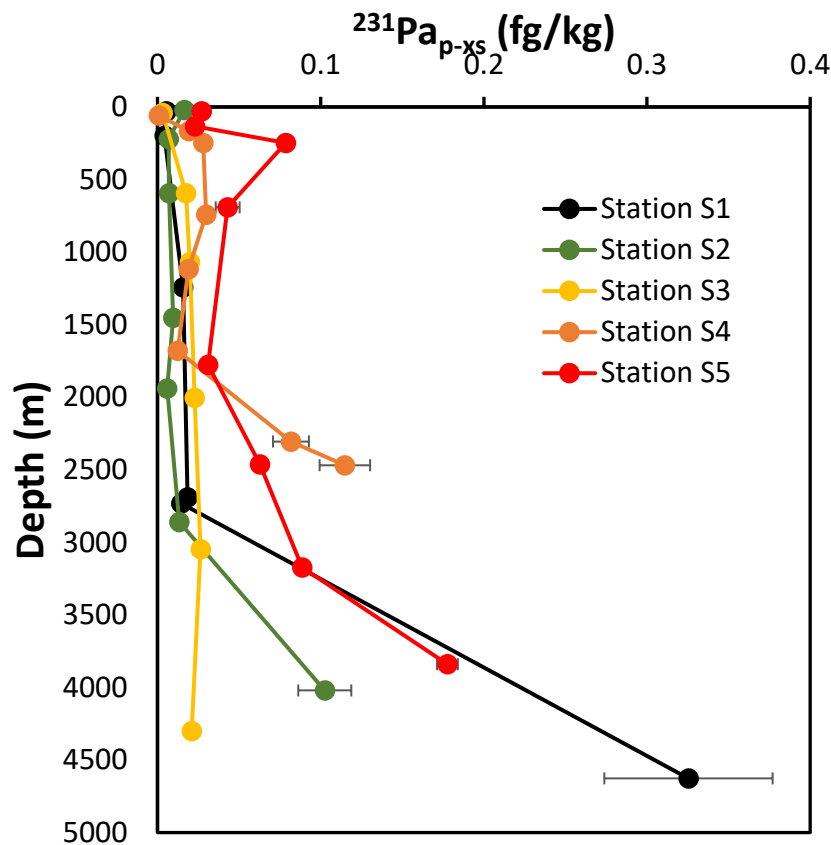


Figure 3 : ²³¹Pa_{xs} concentration in the particulate phase of the super stations of the Bonus GoodHope cruise

4. Discussion

4.1. Dissolved ²³¹Pa in the Weddell Gyre

Dissolved ²³¹Pa profiles are variable in the Weddell Gyre (Rutgers van der Loeff et al., 2016). The cyclonic circulation in the Weddell isolates an inner zone with high ²³¹Pa_{d-xs} concentrations (up to 5.50 ± 0.31 fg/kg, at station 131 of Rutgers van der Loeff, 2016) whereas the rim has lower concentrations (about 4.14 ± 0.51 fg/kg, at station 161 of Rutgers van der Loeff, 2016). The reasons for this concentration gradient are unclear. The low dissolved ²³¹Pa_{xs} measured at Station S5, is in line with the peripheral location of the station in the gyre at the boundary between the Weddell gyre and the southern area of the ACC. This region has a strong gradients, with a enriched concentration in Weddell gyre compare to the ACC, for several radioactive isotopes like ²³⁰Th, ²³²Th, ²³¹Pa (Rutgers van der Loeff et al., 2016; Venchiarutti et al., 2011) or Pb (Boye et al., 2012).

Station S5 and station PS63-161 of ZeroDrake cruise located 150 km further south show a

strong difference in $^{231}\text{Pa}_{\text{xs}}$ concentration despite being in the same hydrological settings (Figure 4). Difference in $^{231}\text{Pa}_{\text{xs}}$ content between these stations could have different origins:

Deep water in the Weddell gyre, WSDW is newly formed deep water in Weddell Sea were reflected by the highly oxygenated signature (about 250 $\mu\text{mol/L}$). The dissolved oxygen in bottom water of station S5 ($\text{O}_2 = 248.3 \mu\text{mol/kg}$, (Branellec et al., 2010) is higher than at ZeroDrake station 131 ($\text{O}_2 = 241.7 \mu\text{mol/kg}$) (Fahrbach & Baar, 2010), suggesting a younger water at station S5 (Figure). Assuming an oxygen utilization rate (OUR) of about 0.12-0.14 $\mu\text{mol/L/y}$ (Broecker et al., 1991; Feely et al., 2004), it would take about 50 y to produce the observed O_2 deficiency of $\sim 7 \mu\text{mol/L}$ observed at station 131. We note that the difference of $^{231}\text{Pa}_{\text{d-xs}}$ between station S5 and station 131 of about 2 fg/kg would take about 80 y at to build up by in situ decay of ^{235}U ($\sim 0.025 \text{ fg/kg/y}$) at station 131 which is of the same order of magnitude than age difference calculated from the oxygen data.

Neodymium isotopes also support the occurrence of difference water masses in the deep water at station S5 and 131. There is a significant difference (1 epsilon unit) of the Nd signature of deep water from station S5 (-10 ± 0.4 at 3900m and 10.1 ± 0.5 at 3150m) (Garcia-Solsona et al., 2014) and 131 (around -9.5 ± 0.3 at 3900m and 9 ± 0.5 at 3000m) (Stichel et al., 2012). The Nd signature at station S5 highlights an imprint of the Weddell shelf sediment signature ($\epsilon_{\text{Nd}} = -15$; Robinson et al., 2021) on the incoming WDW ($\epsilon_{\text{Nd}} = -9.5$ at 3000m at station 161 Stichel et al., 2012a). In contrast, the signature at station 131 reflects the larger fraction of the incoming CDW ($\epsilon_{\text{Nd}} = -8.4$) (Amakawa et al., 2019) in the water recirculating in the Weddell gyre ($\epsilon_{\text{Nd}} = -10$).

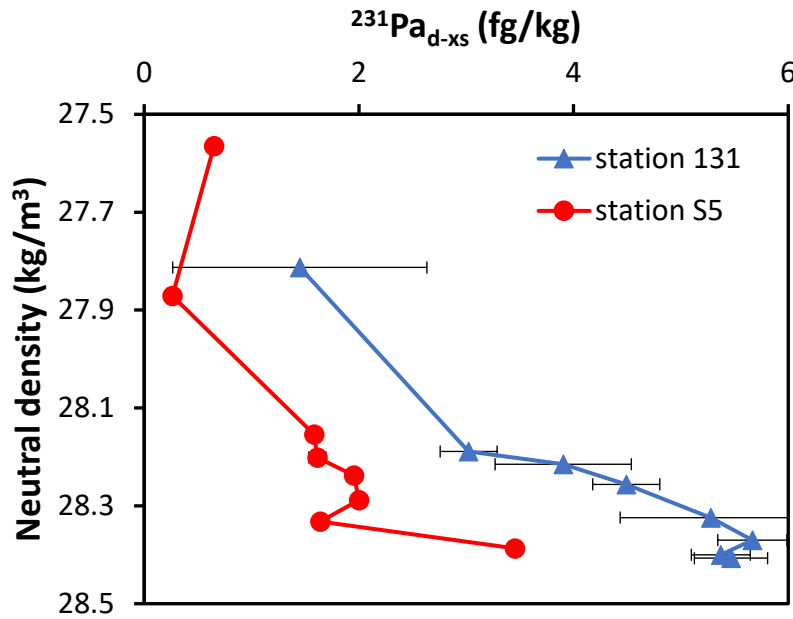


Figure 4 : $^{231}\text{Pa}_{xs-total}$ versus neutral density in the Weddell gyre during the Bonus GoodHope and ZeroDrake cruises. Red dot: station S5 BGH; blue triangle: station 131 of ZeroDrake

4.2. ^{231}Pa and Si behavior across the ACC

^{231}Pa and ^{230}Th have different affinity for the different phases of marine particles, The differential scavenging of these two radionuclides is characterized by the fractionation factor ($F_{\text{Th}/\text{Pa}}$) definee as:

$$F_{\text{Th}/\text{Pa}} = \frac{\left(\frac{^{231}\text{Pa}_{xs}}{^{230}\text{Th}_{xs}}\right)_{\text{diss}}}{\left(\frac{^{231}\text{Pa}_{xs}}{^{230}\text{Th}_{xs}}\right)_{\text{part}}} \quad (3.2)$$

Thorium data were measured on the same seawater samples as ^{231}Pa (Roy-Barman et al., 2019). $F_{\text{Th}/\text{Pa}}$ across the ACC range from 0.57 ± 0.06 in shallow water of station S5 to 37.6 ± 16.2 at 1450 m depth at station S2 (Figure 5; Table ES1). There is a latitudinal gradient from the north of the ACC, with $F_{\text{Th}/\text{Pa}}$ ranging from about 1 in surface waters to about 20 in deep waters, to the south of the polar front with $F_{\text{Th}/\text{Pa}}$ close to 1 throughout the water column, consistent with previous observations across the ACC (Chase et al., 2002; Venchiarutti et al., 2011; Walter et al., 1997).

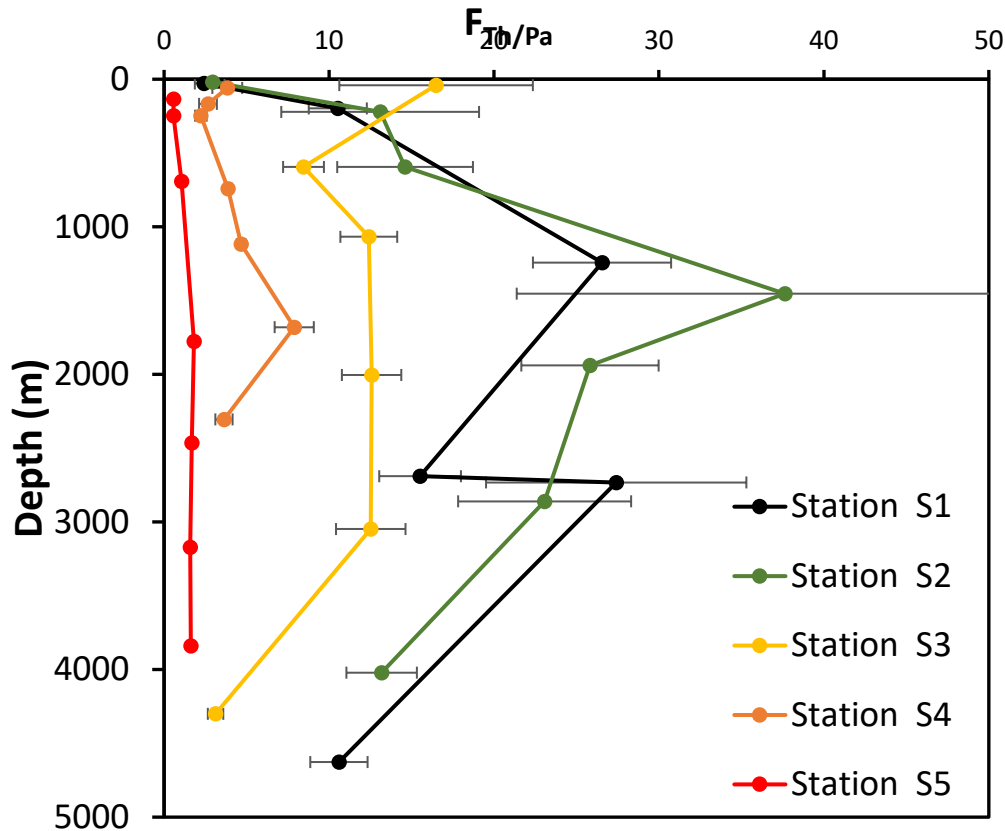


Figure 5 : $F_{Th/Pa}$ fractionation factor profiles. The dissolved concentration was interpolated linearly between two measured point on neutral density basis at depths where particulate concentration was measured. $F_{Th/Pa}$ uncertainties are propagated and expressed in $2\sigma_n$

The variation of $F_{Th/Pa}$ is mainly constrained by the marine particle composition. In polar areas, most of these variations are attributed to the Pa scavenging that is driven by the biogenic silica (BSi) cycle, because ^{231}Pa has a high affinity for biogenic silica (Chase et al., 2002; Gdaniec et al., 2020; Walter et al., 1997). Therefore, we compare the ^{231}Pa and Si concentrations in dissolved and particulate fractions (Figure 6a).

South of the Polar Front, the low $^{231}\text{Pa}_d/\text{DSi}$ ratio in shallow waters is due to the preferential removal of ^{231}Pa relative to the Si, due to particles with high Pa/BSi ratio and the high DSi concentration in these surface waters (Sarmiento et al., 2004). In contrast, north of the Polar Front, water are poor in DSi (Sarmiento et al., 2004) resulting of low BSi production and low Pa removal in shallow waters. In deep waters, the difference of Pa_d/DSi ratio north and south to the Polar Front results from the different compositions of sinking particles: south of the Polar Front, BSi-rich particles release more DSi than BSi-poor particles sinking north to the Polar Front. The general trend of increasing Pa_p/BSi ratio with depth (Figure 6b) reflects the

dissolution of BSi as particles sink through the water column. Meanwhile, ^{231}Pa remains on particles and additional Pa might be scavenged at depth. These observations are consistent with the assumption that the ^{231}Pa is driven by the silicium cycle and the explanation of the meridional gradient given previously (Rutgers van der Loeff et al., 2016).

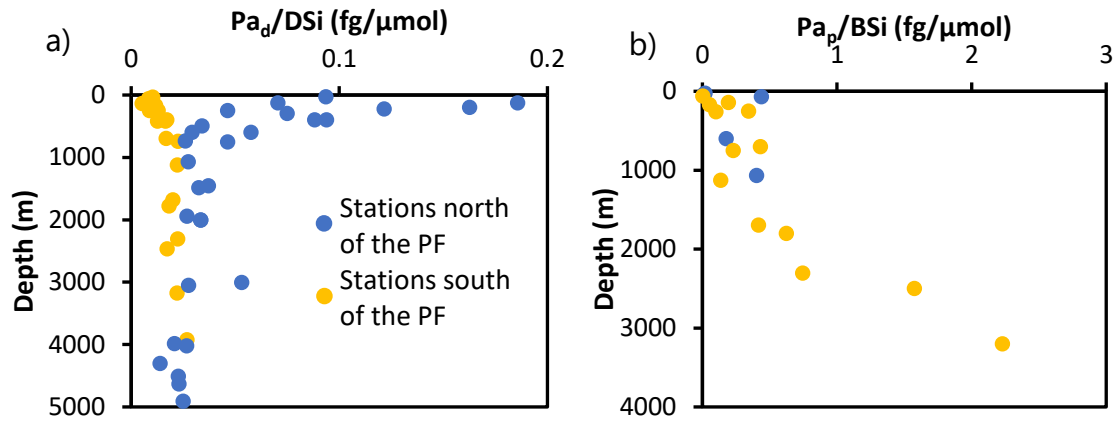


Figure 6 : (a) Pa_d/Si ratio in the water column. (b) Pa_p/BSi ratio in the particulate fraction

Since the $F_{\text{Th}/\text{Pa}}$ seems to be mainly impacted by the affinity of ^{231}Pa for the biogenic silica, we use this new dataset to constrain the partition coefficient of ^{231}Pa on opal in the suspended particle pool. The partition coefficient is defined as the concentration adsorbed on particles normalized by to the dissolved concentration (Hayes et al., 2015):

$$K_{d-\text{bulk}}(X) = \frac{X_{\text{ads}}}{X_{\text{diss}}} \times \frac{1}{\text{SPM}} = \frac{X_{\text{ads}}}{X_{\text{diss}} \text{SPM}} \quad (3.3)$$

Where X represents ^{231}Pa or ^{230}Th , in the adsorbed fraction (\sim particulate concentration) and dissolved fraction, and SPM the mass of suspended particle matter in seawater, that we estimated as the sum of the opal, carbonate, particulate organic matter (POM) and lithogenic matter. The opal mass in particle matter is estimated from the BSi concentration (Fripiat et al., 2011) with the mean opal molar mass ($\text{SiO}_2 \cdot 0.4(\text{H}_2\text{O})$). The carbonate (CaCO_3) concentration was estimated from the particulate Ca concentration (Table . ES4). POM mass was approximated from the particulate organic carbon (POC) (Cavagna et al., 2013) with $\text{POM} = 2 \times \text{POC}$ (Winogradow et al., 2019). The lithogenic matter was approximated from the ^{232}Th particulate concentration (Roy-Barman et al., 2019) with ^{232}Th concentration in lithogenic matter is about 10 ppm.

$K_{d-bulk}(Pa)$ and $K_{d-bulk}(Th)$ were calculated for sample where BSi concentrations were available. The $K_{d-bulk}(Pa)$ range from 0.062 to 2.79×10^6 g/g, and $K_{d-bulk}(Th)$ range from 0.212 to 9.92×10^6 g/g. ^{231}Pa concentration is assumed to be driven by the Si biogeochemical cycle, but there is only a weak correlation between the $K_{d-bulk}(Pa)$ of Bonus particles and the BSi proportion in marine particles ($R^2 = 0.17$), and no correlation with the $K_{d-bulk}(Th)$ ($R^2 = 0.02$) (Figure). The $K_{d-opal}(Pa)$ can be deduced from $K_{d-bulk}(Pa)$ as follows:

$$K_{d-opal} = \frac{(K_{d-bulk} - f_{litho} \times K_{d-litho} - f_{CaCO_3} \times K_{d-CaCO_3} - f_{POM} \times K_{d-POM})}{f_{opal}} \quad (3.4)$$

Where f_{litho} , f_{CaCO_3} , f_{opal} and f_{POM} are the mass fractions of each phase in seawater, $K_{d-litho}$, K_{d-CaCO_3} and K_{d-POM} are the partition coefficient of each phase, with respective values : 2.3×10^6 ; 0.9×10^6 and 0.2×10^6 , determined on North Atlantic particles (Hayes et al., 2015). Taking into account only particulate samples containing more than 50% of BSi (samples from opal belt and south of the polar front) to avoid uncertainties amplification for BSi-poor samples, we obtain $K_{d-opal}(Pa) = 1.42 \pm 0.55 \times 10^6$ g/g (1 standard error). The same approach applied to the $K_{d-opal}(Th)$ provide no significant results, probably because $K_{d-opal}(Th)$ is in the same range or lower than the K_d of the other phases.

$K_{d-opal}(Pa)$ crude estimation on suspended particles are in the upper range of previous estimation made on sediment trap material ($K_{d-opal}(Pa) = 1.0$ to 1.4×10^6 , Chase et al., 2002; Li, 2005; Luo and Ku, 2004), and over the estimation made on SiO_2 from diatoms in laboratory experiment ($K_{d-opal}(Pa) = 1.9 \times 10^5$, Lin et al., 2014 ; $K_{d-opal}(Pa) = 5.0 \times 10^5$, Geibert and Usbeck, 2004). *In situ* material, suspended particles or sediment trap, have a larger partition coefficient than laboratory experiment on diatoms culture. This value confirms that opal represents a significant contribution to the ^{231}Pa scavenging, essentially with the opal dominance in particle matter in Southern Ocean.

4.3. Isopycnal transport and scavenging of ^{231}Pa across the ACC

Across the ACC, ^{230}Th concentrations were shown to be relatively conservative along isopycnal surfaces (Roy-Barman et al., 2019; Rutgers van der Loeff and Berger, 1993). Thorium isotopes transport along the BGH section was represented with an advection-diffusion-scavenging

model along isopycnal surfaces (Figure 7). This allowed linking tracers (θ -S- ^{230}Th - ^{232}Th) and estimating transport parameters (Roy-Barman et al., 2019). The transports are not assumed to be a true meridional mixing along the BGH section, but it allows to estimate the residual meridional component of the mixing (advection, diffusion) embedded in the dominant zonal of the ACC Atlantic sector. In the present study, we report that ^{231}Pa concentrations show the same behavior than ^{230}Th , with relatively small gradients along the a given isopycnal surfaces (Figure 8). Therefore, we now use ^{231}Pa data as additional constrain to the model, test its robustness and the effect of an additional equation on the estimation of transport parameters.

As for Th isotopes, we focus on two isopycnal surfaces defined by $\gamma_n = 27.865 \text{ kg/m}^3$ and $\gamma_n = 28.094 \text{ kg/m}^3$ (fig. 7). The first isopycnal surface ($\gamma_n = 27.865 \text{ kg/m}^3$) corresponds to the mixing of the UCDW at station S1 at around a depth of 1500 m and the D-UCDW at station S4 with the isopycnal surface upwells to about 200m. The second isopycnal surface ($\gamma_n = 28.094 \text{ kg/m}^3$), in the southern part of the ACC, corresponds to the mixing between the upper part of the NADW at the station S3 at a depth of about 2500m and the WDW at station S5, at a depth of about 150m. These 2 isopycnal surfaces were chosen because along the Bonus Good Hope section they best correspond to a 2 water masses mixing as indicated by θ -S data.

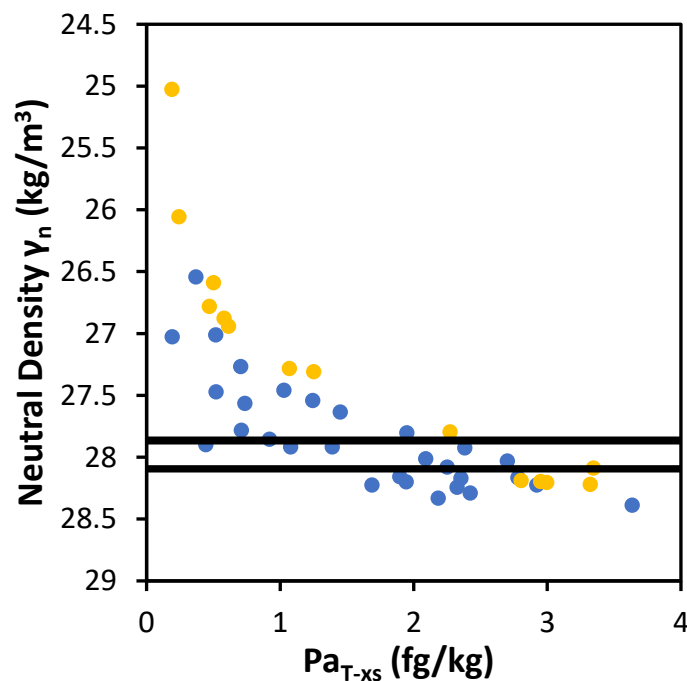


Figure 7 : Distribution of the $^{231}\text{Pa}_t$ ($\text{Pa}_d + \text{Pa}_p$) concentration from the Bonus GoodHope cruise against the neutral density. The studied isopycnal surfaces ($\gamma_n = 27.865 \text{ kg/m}^3$ and $\gamma_n = 28.094 \text{ kg/m}^3$) are highlighted by black lines.

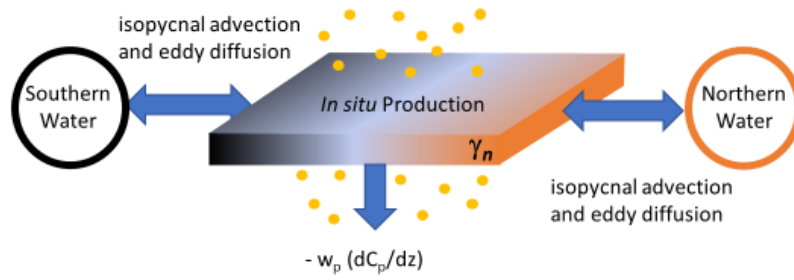


Figure 8 : Conceptual diagram of the advection-diffusion-scavenging model

Assuming steady state, the transport equation along an isopycnal surface (Roy-Barman et al., 2019) is given by :

$$K_i \frac{\partial^2 C_t}{\partial x^2} - u_i \frac{\partial C_t}{\partial x} + P_d - w_p \left(\frac{\partial C_p}{\partial z} \right) = 0 \quad (3.5)$$

Where K_i and u_i are respectively the cross-stream eddy diffusion coefficient and the cross-stream isopycnal advection velocity coefficient. P_d is the *in situ* production of the radiogenic element and w_p the settling speed of particles. C_t and C_p are respectively the total concentration and the particulate concentration of the radiogenic element.

The x-axis is parallel to the isopycnal surface in the meridional direction and oriented northward. The z-axis is oriented perpendicular to the isopycnal surface and hence is almost vertical. Just like in the reversible scavenging model, keeping w_p out of the partial derivative requires to assume that w_p does not vary with z. The Eq. (3.5) was integrated along the isopycnal surface of the BGH section between the stations corresponding to the end members of water mass mixing (stations for S1 and S4 for $\gamma_n=27.865 \text{ kg/m}^3$, from the I-UCDW to the DP-UCDW and S3 and S5 for $\gamma_n=28.094 \text{ kg/m}^3$, from the SW-NADW/AABW to the AASW/WW). This is a simplified view of water transport because while water moves across the ACC, it is also rapidly advected eastward by the ACC (S2–S4) and the northern limb of the Weddell Gyre (S5). We assume that K_i , u_i , w_p and (dC_p/dz) are all constant along x in order to obtain analytical solutions. We note $C_t=C_{t\text{-cons}} + \Delta C_t$, where $C_{t\text{-cons}}$ is the concentration of the tracer if it behaves as a conservative mixing (only mixing by advection and diffusion) and ΔC_t is the deviation of this tracer due to the radioactive production and scavenging on settling particles. The solution is then:

$$C_{t-conc} = \frac{\frac{u_i}{K_i}x - e^{\frac{u_i}{K_i}x_B}}{\frac{u_i}{K_i}x_A - e^{\frac{u_i}{K_i}x_B}} (C_{t_A} - C_{t_B}) + C_{t_B} \quad (3.6)$$

$$\Delta C_t = \frac{\left(P_d - w_p \frac{dC_p}{dz} \right)}{u} \left((x - x_B) + (x_B - x_A) \left(\frac{\frac{u_i}{K_i}x - e^{\frac{u_i}{K_i}x_B}}{\frac{u_i}{K_i}x_A - e^{\frac{u_i}{K_i}x_B}} \right) \right) \quad (3.7)$$

Where the suffixes A and B represents the end-member stations and x the latitudinal position.

For a conservative tracer such as the salinity (S), the concentration is given by:

$$S = \frac{e^{\frac{u_i}{K_i}(x-x_A)} - 1}{e^{\frac{u_i}{K_i}(x_B-x_A)} - 1} (S_B - S_A) + S_A \quad (3.8)$$

This equation allows to determine $u_i/K_i \approx -1.6 \cdot 10^{-6} \text{ m}^{-1}$ for both isopycnal surfaces (Roy-Barman et al., 2019). Then equations 3.6 and 3.7 were applied to ^{230}Th and ^{232}Th to derive a first estimate of the transport parameters (Table 1, see Roy-Barman et al., 2019 for details of the calculations). Finally, we applied the equations 3.6 and 3.7 were to ^{230}Th and ^{232}Th and ^{231}Pa data of the BGH cruise to obtain a second set of transport parameters (Table 1)

We use a Monte-Carlo simulation (n=50000) over the 3 model parameters (u_i , K_i , w_p) with a large dispersion of the their a priori values. Further constrains on u_i and K_i arise from the u_i/K_i ratio solution of the conservative equation. A priori values of dC_p/dt covers all the particulate gradients measured along the isopycnals. We determine the coefficient of determination (R^2) between each mixing curves of the Monte-Carlo simulations and the measured concentrations on the isopycnal surface. We use the mean of the R^2 on the three isotopes as a selection filter, to keep only parameters values that make converging mixing curves toward the measured concentrations. We arbitrarily put the selection at $R^2 = 0.97$ for the first isopycnal surface ($\gamma_n = 27.865$) and $R^2 = 0.75$ for the second one ($\gamma_n = 28.094$). This selection factor brings a selection of the most fitting parameters, which we derived their mean value and standard deviation (Tab. 1)

Including ^{231}Pa in the model, there is no significant change on the average estimate on parameters K_i and u_i , but the uncertainties are reduced by a factor 2 to 4 (Table 1). Among the model parameters, the particle settling speed is the most affected by the introduction of the Pa constrains with higher settling speed on the isopycnal surface 28.094 kg/m^3 , with a value of $990 \pm 85 \text{ m/y}$ against $674 \pm 250 \text{ m/y}$ with Th isotopes alone (Table 1). This change of settling speed

is calculated with the stations S3 to S5, located on the southern part of the section, where the vertical particulate flux is mainly driven by diatoms (that scavenge Pa efficiently). Hence, ^{231}Pa sensitivity to scavenging by the biogenic silica allows a better representation of these fast sinking particles. Conversely, calculation along the isopycnal surface $\gamma_n = 27.865 \text{ kg/m}^3$ is based more on the northern stations, where lower diatom production does not drive the flux of settling particles. Therefore, including Pa data along this isopycnal surface does not affect the particle settling speed, but significantly reduces the uncertainties on u_i , K_i and w_p . The advection-diffusion-scavenging model is able to reproduce the data measured on sample from the BGH cruise, linearly distribute along an isopycnal surface (Figure 9). This suggests that the model processes are the most predominant on the ^{231}Pa cycle of the ACC and our different hypothesis like the steady state are consistent to explain the observed distribution.

Table 1 : Model parameters and output

γ_n (kg/m^3)	$d^{231}\text{Pa}_p/dz$ (fg/kg/m)	K_i (m^2/s)	u_i (m/s)	w_p (m/y)	Best fit R^2 ^{232}Th	Best fit R^2 ^{230}Th	Best fit R^2 ^{231}Pa
<i>Roy-Barman et al. (2019)</i>							
27.865 (S1-S4)	--	2000 ± 840	- 0.0033 ± 0.0014	674 ± 250	0.994	0.945	
28.094 (S3-S5)	--	2180 ± 480	- 0.0036 ± 0.0008	418 ± 470	0.696	0.806	
<i>This study</i>							
27.865 (S1-S4)	$3.7\text{e-}6$ $\pm 1.9\text{e-}6$	1900 ± 180	- 0.0030 ± 0.0003	990 ± 85	0.994	0.945	0.997
28.094 (S3-S5)	$2.5\text{e-}4$ $\pm 2.3\text{e-}4$	1900 ± 120	- 0.0031 ± 0.0002	370 ± 200	0.0696	0.806	0.922

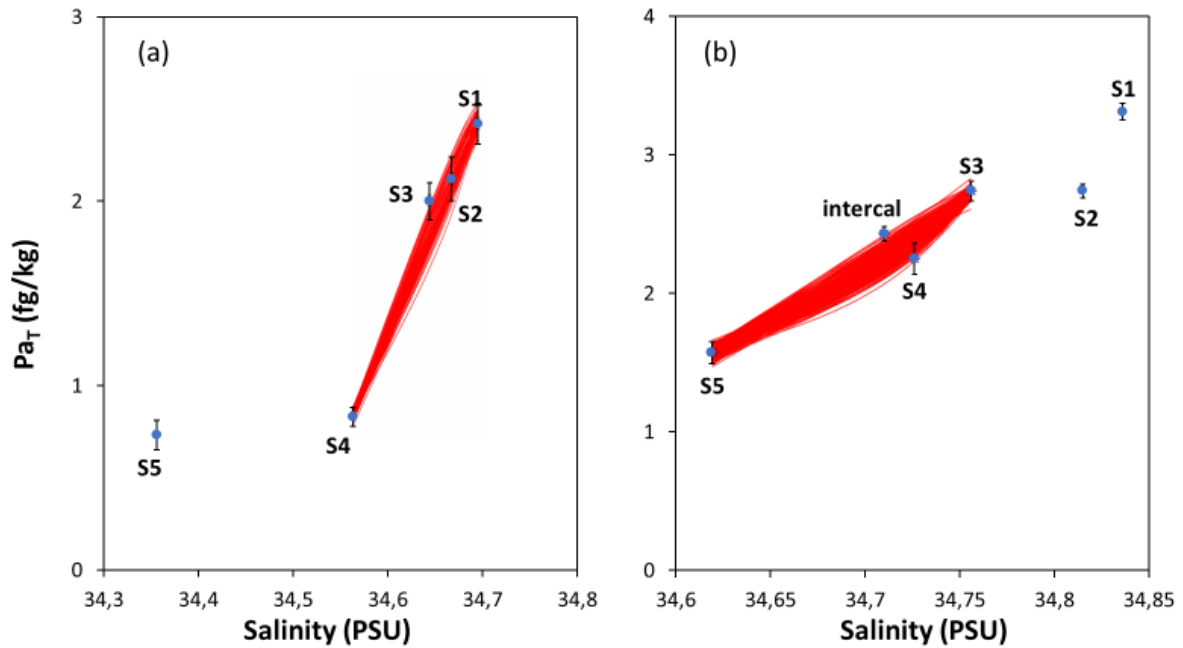


Figure 9 : Advection-diffusion modelling of Salinity and $^{231}\text{Pa}_T$ compared to data, at the isopycnal surface $\gamma_n = 27.865 \text{ kg/m}^3$ (a) and at the isopycnal surface $\gamma_n = 28.094 \text{ kg/m}^3$ (b). Stacked red curves are the fitting curved with the best R^2 obtained with the Monte Carlo simulation.

Having determined the transport parameters, it is now possible to calculate the respective weights of advection, diffusion and particle transport of *in situ* ^{231}Pa production relative the ^{231}Pa *in situ* production (Table) to compare the relative contribution of each flux on the observed ^{231}Pa distribution across the ACC. Hence, crude estimation shows a strong influence of the mixing fluxes (advection ≈ 9 -16 times the production rate and eddy diffusion = 7-20 times the production rate) on the ^{231}Pa distribution across the ACC. By contrast, vertical scavenging represents only 20%-41% of the *in situ* production. The ^{231}Pa particulate flux obtained is significantly larger at the level S1-S3 near the African margin ($\frac{F_{scav}}{F_{prod}} = 41\%$) along $\gamma_n = 27.865 \text{ kg/m}^3$ than at the station S4-S5 in the opal belt ($\frac{F_{scav}}{F_{prod}} = 20\%$) along $\gamma_n = 28.094 \text{ kg/m}^3$ (note that for these 2 isopycnals the mean depth considered is around 1200-1400 m). This reflect that ^{231}Pa is mainly constrained by the advection and diffusion in Southern Ocean although the scavenging flux measured in the opal belt is lower than in water near the African margin.

5. Conclusion

The distribution of ^{231}Pa in the Southern Ocean is mainly constrained isopycnal advection and diffusion. The crude estimation shows that most of the ^{231}Pa transit through the advection and diffusion fluxes and few of the ^{231}Pa is scavenged in the ACC, north to the Polar Front. This makes the ^{231}Pa a good tracer of the mixing in the Southern Ocean and also a chronometer of this mixing, like in Weddell Gyre where we were able to made an estimation of the age difference between the inner and the peripheral Weddell Gyre water. This new dataset of ^{231}Pa in this high latitude area also allowed to propose a new estimate of the ^{231}Pa adsorption coefficient on opal particle fraction which is higher than previous estimations. The use of Pa and Th in the model allowed determining the settling rate of the particles, but large uncertainties remained despite the addition of ^{231}Pa tracer in the advection diffusion scavenging model. The 2 end-member mixing model presented here could be used only for 2 isopycnal surfaces. More complex mixings could be treated through optimum multiparameter (OMP) analysis (Le Roy et al., 2018) when more ^{231}Pa data will be available. Another improvement of the model would be to use a variable particulate flux along the isopycnal surface $\gamma_n=28.094$ kg/kg, where the particulate Pa gradient increases by two order of magnitudes between station S3 (10^{-6} fg/kg/m) and station S5 (10^{-4} fg/kg/m) by crossing the Polar Front, reflecting the change of the particulate phase carrying the ^{231}Pa scavenging. Finally, a last challenge would be to include other mixing tracers in the model such as Nd isotopes for water mass tracing or ^{227}Ra or ^{227}Ac as short-lived chronometers.

Acknowledgements

Authors would like to acknowledge all the on-board crew and sampling team of BGH cruise. This work also supported by the French National program LEFE (Les Enveloppes Fluides et l'Environnement) through support to the AbAc project.

6. References

- Abadie, C., Lacan, F., Radic, A., Pradoux, C., Poitrasson, F., 2017. Iron isotopes reveal distinct dissolved iron sources and pathways in the intermediate versus deep Southern Ocean. *Proc. Natl. Acad. Sci.* 114, 858–863. <https://doi.org/10.1073/pnas.1603107114>
- Amakawa, H., Yu, T.-L., Tazoe, H., Obata, H., Gamo, T., Sano, Y., Shen, C.-C., Suzuki, K., 2019. Neodymium concentration and isotopic composition distributions in the southwestern Indian Ocean and the Indian sector of the Southern Ocean. *Chem. Geol.* 511, 190–203. <https://doi.org/10.1016/j.chemgeo.2019.01.007>
- Anderson, R.F., Fleisher, M.Q., Robinson, L.F., Edwards, R.L., Hoff, J.A., Moran, S.B., Loeff, M.R. van der, Thomas, A.L., Roy-Barman, M., Francois, R., 2012. GEOTRACES intercalibration of ^{230}Th , ^{232}Th , ^{231}Pa , and prospects for ^{10}Be . *Limnol. Oceanogr. Methods* 10, 179–213.

- <https://doi.org/10.4319/lom.2012.10.179>
- Bown, J., Boye, M., Baker, A., Duvieilbourg, E., Lacan, F., Le Moigne, F., Planchon, F., Speich, S., Nelson, D.M., 2011. The biogeochemical cycle of dissolved cobalt in the Atlantic and the Southern Ocean south off the coast of South Africa. *Mar. Chem.* 126, 193–206. <https://doi.org/10.1016/j.marchem.2011.03.008>
- Boye, M., Wake, B.D., Lopez Garcia, P., Bown, J., Baker, A.R., Achterberg, E.P., 2012. Distributions of dissolved trace metals (Cd, Cu, Mn, Pb, Ag) in the southeastern Atlantic and the Southern Ocean (preprint). *Biogeochemistry: Open Ocean*. <https://doi.org/10.5194/bgd-9-3579-2012>
- Branellec, P., Arhan M., Speich S., 2010. Projet GoodHope. Campagne BONUS / GOODHOPE. Rapport de données CTD-O2 . OPS/LPO/10-02
- Broecker, W.S., Blanton, S., Smethie Jr., W.M., Ostlund, G., 1991. Radiocarbon decay and oxygen utilization in the Deep Atlantic Ocean. *Glob. Biogeochem. Cycles* 5, 87–117. <https://doi.org/10.1029/90GB02279>
- Cavagna, A.-J., Dehairs, F., Bouillon, S., Woule-Ebongué, V., Planchon, F., Delille, B., Bouloubassi, I., 2013. Water column distribution and carbon isotopic signal of cholesterol, brassicasterol and particulate organic carbon in the Atlantic sector of the Southern Ocean. *Biogeosciences* 10, 2787–2801. <https://doi.org/10.5194/bg-10-2787-2013>
- Chase, Z., Anderson, R.F., Fleisher, M.Q., Kubik, P.W., 2002. The influence of particle composition and particle flux on scavenging of Th, Pa and Be in the ocean. *Earth Planet. Sci. Lett.* 15.
- Chever, F., Bucciarelli, E., Sarthou, G., Speich, S., Arhan, M., Penven, P., Tagliabue, A., 2010. Physical speciation of iron in the Atlantic sector of the Southern Ocean along a transect from the subtropical domain to the Weddell Sea Gyre. *J. Geophys. Res. Oceans* 115. <https://doi.org/10.1029/2009JC005880>
- Condon, D.J., McLean, N., Noble, S.R., Bowring, S.A., 2010. Isotopic composition ($^{238}\text{U}/^{235}\text{U}$) of some commonly used uranium reference materials. *Geochim. Cosmochim. Acta* 74, 7127–7143. <https://doi.org/10.1016/j.gca.2010.09.019>
- Deacon, G.E.R., 1979. The Weddell gyre. *Deep Sea Res. Part Oceanogr. Res. Pap.* 26, 981–995. [https://doi.org/10.1016/0198-0149\(79\)90044-X](https://doi.org/10.1016/0198-0149(79)90044-X)
- DeMaster, D.J., 1981. The supply and accumulation of silica in the marine environment. *Geochim. Cosmochim. Acta* 45, 1715–1732. [https://doi.org/10.1016/0016-7037\(81\)90006-5](https://doi.org/10.1016/0016-7037(81)90006-5)
- Fahrbach, E., 2010. ANT-XXIV/3 report, O2 CTD report, p78-84, hdl:10013/epic.34050
- Feely, R.A., Sabine, C.L., Schlitzer, R., Bullister, J.L., Mecking, S., Greeley, D., 2004. Oxygen Utilization and Organic Carbon Remineralization in the Upper Water Column of the Pacific Ocean. *J. Oceanogr.* 60, 45–52. <https://doi.org/10.1023/B:JOCE.0000038317.01279.aa>
- Fripiat, F., Cavagna, A.-J., Dehairs, F., Speich, S., André, L., Cardinal, D., 2011. Silicon pool dynamics and biogenic silica export in the Southern Ocean inferred from Si-isotopes. *Ocean Sci.* 7, 533–547. <https://doi.org/10.5194/os-7-533-2011>
- Garcia-Solsona, E., Jeandel, C., Labatut, M., Lacan, F., Vance, D., Chavagnac, V., Pradoux, C., 2014. Rare earth elements and Nd isotopes tracing water mass mixing and particle-seawater interactions in the SE Atlantic. *Geochim. Cosmochim. Acta* 125, 351–372. <https://doi.org/10.1016/j.gca.2013.10.009>
- Gdaniec, S., Roy-Barman, M., Foliot, L., Thil, F., Dapoigny, A., Burckel, P., Garcia-Orellana, J., Masqué, P., Mörth, C.-M., Andersson, P.S., 2018. Thorium and protactinium isotopes as tracers of marine particle fluxes and deep water circulation in the Mediterranean Sea. *Mar. Chem.* 199, 12–23. <https://doi.org/10.1016/j.marchem.2017.12.002>
- Gdaniec, S., Roy-Barman, M., Levier, M., Valk, O., van der Loeff, M.R., Foliot, L., Dapoigny, A., Missiaen, L., Mörth, C.-M., Andersson, P.S., 2020. ^{231}Pa and ^{230}Th in the Arctic Ocean: Implications for boundary scavenging and $^{231}\text{Pa}/^{230}\text{Th}$ fractionation in the Eurasian Basin. *Chem. Geol.* 532, 119380. <https://doi.org/10.1016/j.chemgeo.2019.119380>
- Geibert, W., Usbeck, R., 2004. Adsorption of thorium and protactinium onto different particle types: experimental findings 11 Associate editor: S. Krishnaswami. *Geochim. Cosmochim. Acta* 68, 1489–1501. <https://doi.org/10.1016/j.gca.2003.10.011>
- Ghaleb, B., Pons-Branchu, E., Deschamps, P., 2004. Improved method for radium extraction from environmental samples and its analysis by thermal ionization mass spectrometry. *J. Anal. At. Spectrom.* 19, 906. <https://doi.org/10.1039/b402237h>

- Gouretski, V.V., Danilov, A.I., 1993. Weddell Gyre: structure of the eastern boundary. *Deep Sea Res. Part Oceanogr. Res. Pap.* 40, 561–582. [https://doi.org/10.1016/0967-0637\(93\)90146-T](https://doi.org/10.1016/0967-0637(93)90146-T)
- Guihou, A., Pichat, S., Nave, S., Govin, A., Labeyrie, L., Michel, E., Waelbroeck, C., 2010. Late slowdown of the Atlantic Meridional Overturning Circulation during the Last Glacial Inception: New constraints from sedimentary ($^{231}\text{Pa}/^{230}\text{Th}$). *Earth Planet. Sci. Lett.* 289, 520–529. <https://doi.org/10.1016/j.epsl.2009.11.045>
- Hayes, C.T., Anderson, R.F., Fleisher, M.Q., Vivancos, S.M., Lam, P.J., Ohnemus, D.C., Huang, K.-F., Robinson, L.F., Lu, Y., Cheng, H., Edwards, R.L., Moran, S.B., 2015. Intensity of Th and Pa scavenging partitioned by particle chemistry in the North Atlantic Ocean. *Mar. Chem.* 170, 49–60. <https://doi.org/10.1016/j.marchem.2015.01.006>
- Jeandel, C., Venchiarutti, C., Bourquin, M., Pradoux, C., Lacan, F., Beek, P. van, Riotte, J., 2011. Single Column Sequential Extraction of Ra, Nd, Th, Pa and U from a Natural Sample. *Geostand. Geoanalytical Res.* 35, 449–459. <https://doi.org/10.1111/j.1751-908X.2010.00087.x>
- Le Roy, E., Sanial, V., Charette, M.A., van Beek, P., Lacan, F., Jacquet, S.H.M., Henderson, P.B., Souhaut, M., García-Ibáñez, M.I., Jeandel, C., Pérez, F.F., Sarthou, G., 2018. The ^{226}Ra –Ba relationship in the North Atlantic during GEOTRACES-GA01. *Biogeosciences* 15, 3027–3048. <https://doi.org/10.5194/bg-15-3027-2018>
- Levier, M., Roy-Barman, M., Colin, C., Dapoigny, A., 2021. Determination of low level of actinium 227 in seawater and freshwater by isotope dilution and mass spectrometry. *Mar. Chem.* 233, 103986. <https://doi.org/10.1016/j.marchem.2021.103986>
- Li, Y.-H., 2005. Controversy over the relationship between major components of sediment-trap materials and the bulk distribution coefficients of ^{230}Th , ^{231}Pa , and ^{10}Be . *Earth Planet. Sci. Lett.* 233, 1–7. <https://doi.org/10.1016/j.epsl.2005.02.023>
- Lin, P., Guo, L., Chen, M., 2014. Adsorption and fractionation of thorium and protactinium on nanoparticles in seawater. *Mar. Chem.* 162, 50–59. <https://doi.org/10.1016/j.marchem.2014.03.004>
- Livermore, B.D., Connelly, J.N., Moynier, F., Bizzarro, M., 2018. Evaluating the robustness of a consensus $^{238}\text{U}/^{235}\text{U}$ value for U-Pb geochronology. *Geochim. Cosmochim. Acta* 237, 171–183. <https://doi.org/10.1016/j.gca.2018.06.014>
- Luo, S., Ku, T.-L., 2004. On the importance of opal, carbonate, and lithogenic clays in scavenging and fractionating ^{230}Th , ^{231}Pa and ^{10}Be in the ocean. *Earth Planet. Sci. Lett.* 220, 201–211. [https://doi.org/10.1016/S0012-821X\(04\)00027-5](https://doi.org/10.1016/S0012-821X(04)00027-5)
- Marshall, J., Speer, K., 2012. Closure of the meridional overturning circulation through Southern Ocean upwelling. *Nat. Geosci.* 5, 171–180. <https://doi.org/10.1038/ngeo1391>
- Nicholls, K.W., Østerhus, S., Makinson, K., Gammelsrød, T., Fahrbach, E., 2009. Ice-ocean processes over the continental shelf of the southern Weddell Sea, Antarctica: A review. *Rev. Geophys.* 47, RG3003. <https://doi.org/10.1029/2007RG000250>
- Pavia, F.J., Anderson, R.F., Pinedo-Gonzalez, P., Fleisher, M.Q., Brzezinski, M.A., Robinson, R.S., 2020. Isopycnal Transport and Scavenging of ^{230}Th and ^{231}Pa in the Pacific Southern Ocean. *Glob. Biogeochem. Cycles* 34. <https://doi.org/10.1029/2020GB006760>
- Robinson, S., Ivanovic, R., van de Flierdt, T., Blanchet, C.L., Tachikawa, K., Martin, E.E., Cook, C.P., Williams, T., Gregoire, L., Plancherel, Y., Jeandel, C., Arsouze, T., 2021. Global continental and marine detrital ϵNd : An updated compilation for use in understanding marine Nd cycling. *Chem. Geol.* 567, 120119. <https://doi.org/10.1016/j.chemgeo.2021.120119>
- Roy-Barman, M., Thil, F., Bordier, L., Dapoigny, A., Foliot, L., Ayrault, S., Lacan, F., Jeandel, C., Pradoux, C., Garcia-Solsona, E., 2019. Thorium isotopes in the Southeast Atlantic Ocean: Tracking scavenging during water mass mixing along neutral density surfaces. *Deep Sea Res. Part Oceanogr. Res. Pap.* 149, 103042. <https://doi.org/10.1016/j.dsr.2019.05.002>
- Rutgers van der Loeff, M., Moore, W.S., 1999. Determination of natural radioactive tracers., in: *Methods of Seawater Analysis*. pp. 365–397.
- Rutgers van der Loeff, M., Venchiarutti, C., Stimac, I., van Ooijen, J., Huhn, O., Rohardt, G., Strass, V., 2016. Meridional circulation across the Antarctic Circumpolar Current serves as a double ^{231}Pa and ^{230}Th trap. *Earth Planet. Sci. Lett.* 455, 73–84. <https://doi.org/10.1016/j.epsl.2016.07.027>
- Rutgers van der Loeff, M.M., Berger, G.W., 1993. Scavenging of ^{230}Th and ^{231}Pa near the antarctic polar

- front in the South Atlantic. *Deep Sea Res. Part Oceanogr. Res. Pap.* 40, 339–357. [https://doi.org/10.1016/0967-0637\(93\)90007-P](https://doi.org/10.1016/0967-0637(93)90007-P)
- Ryan, S., Schröder, M., Huhn, O., Timmermann, R., 2016. On the warm inflow at the eastern boundary of the Weddell Gyre. *Deep Sea Res. Part Oceanogr. Res. Pap.* 107, 70–81. <https://doi.org/10.1016/j.dsr.2015.11.002>
- Sarmiento, J.L., Gruber, N., Brzezinski, M.A., Dunne, J.P., 2004. High-latitude controls of thermocline nutrients and low latitude biological productivity. *Nature* 427, 56–60. <https://doi.org/10.1038/nature02127>
- Scholten, J.C., Fietzke, J., Mangini, A., Garbe-Schönberg, C.-D., Eisenhauer, A., Schneider, R., Stoffers, P., 2008. Advection and scavenging: Effects on ^{230}Th and ^{231}Pa distribution off Southwest Africa. *Earth Planet. Sci. Lett.* 271, 159–169. <https://doi.org/10.1016/j.epsl.2008.03.060>
- Schröder, M., Fahrback, E., 1999. On the structure and the transport of the eastern Weddell Gyre. *Deep Sea Res. Part II Top. Stud. Oceanogr.* 46, 501–527. [https://doi.org/10.1016/S0967-0645\(98\)00112-X](https://doi.org/10.1016/S0967-0645(98)00112-X)
- Sokolov, S., Rintoul, S.R., 2009. Circumpolar structure and distribution of the Antarctic Circumpolar Current fronts: 1. Mean circumpolar paths. *J. Geophys. Res. Oceans* 114. <https://doi.org/10.1029/2008JC005108>
- Stichel, T., Frank, M., Rickli, J., Hathorne, E.C., Haley, B.A., Jeandel, C., Pradoux, C., 2012a. Sources and input mechanisms of hafnium and neodymium in surface waters of the Atlantic sector of the Southern Ocean. *Geochim. Cosmochim. Acta* 94, 22–37. <https://doi.org/10.1016/j.gca.2012.07.005>
- Vencharutti, C., van der Loeff, M.R., Stimac, I., 2011. Scavenging of ^{231}Pa and thorium isotopes based on dissolved and size-fractionated particulate distributions at Drake Passage (ANTXXIV-3). *Deep Sea Res. Part II Top. Stud. Oceanogr., Physics, Carbon Dioxide, Trace Elements and Isotopes in the Southern Ocean: The Polarstern Expeditions ANT XXIV-3 (2008) and ANT XXIII/3 (2006)* 58, 2767–2784. <https://doi.org/10.1016/j.dsr2.2010.10.040>
- Walter, H.J., Rutgers van der Loeff, M.M., Hoeltzen, H., 1997. Enhanced scavenging of ^{231}Pa relative to ^{230}Th in the South Atlantic south of the Polar Front: Implications for the use of the $^{231}\text{Pa}/^{230}\text{Th}$ ratio as a paleoproductivity proxy. *Earth Planet. Sci. Lett.* 149, 85–100. [https://doi.org/10.1016/S0012-821X\(97\)00068-X](https://doi.org/10.1016/S0012-821X(97)00068-X)
- Winogradow, A., Mackiewicz, A., Pempkowiak, J., 2019. Seasonal changes in particulate organic matter (POM) concentrations and properties measured from deep areas of the Baltic Sea. *Oceanologia* 61, 505–521. <https://doi.org/10.1016/j.oceano.2019.05.004>
- Yu, E.-F., Francois, R., Bacon, M.P., 1996. Similar rates of modern and last-glacial ocean thermohaline circulation inferred from radiochemical data. *Nature* 379, 689–694. <https://doi.org/10.1038/379689a0>

Electronic Support :

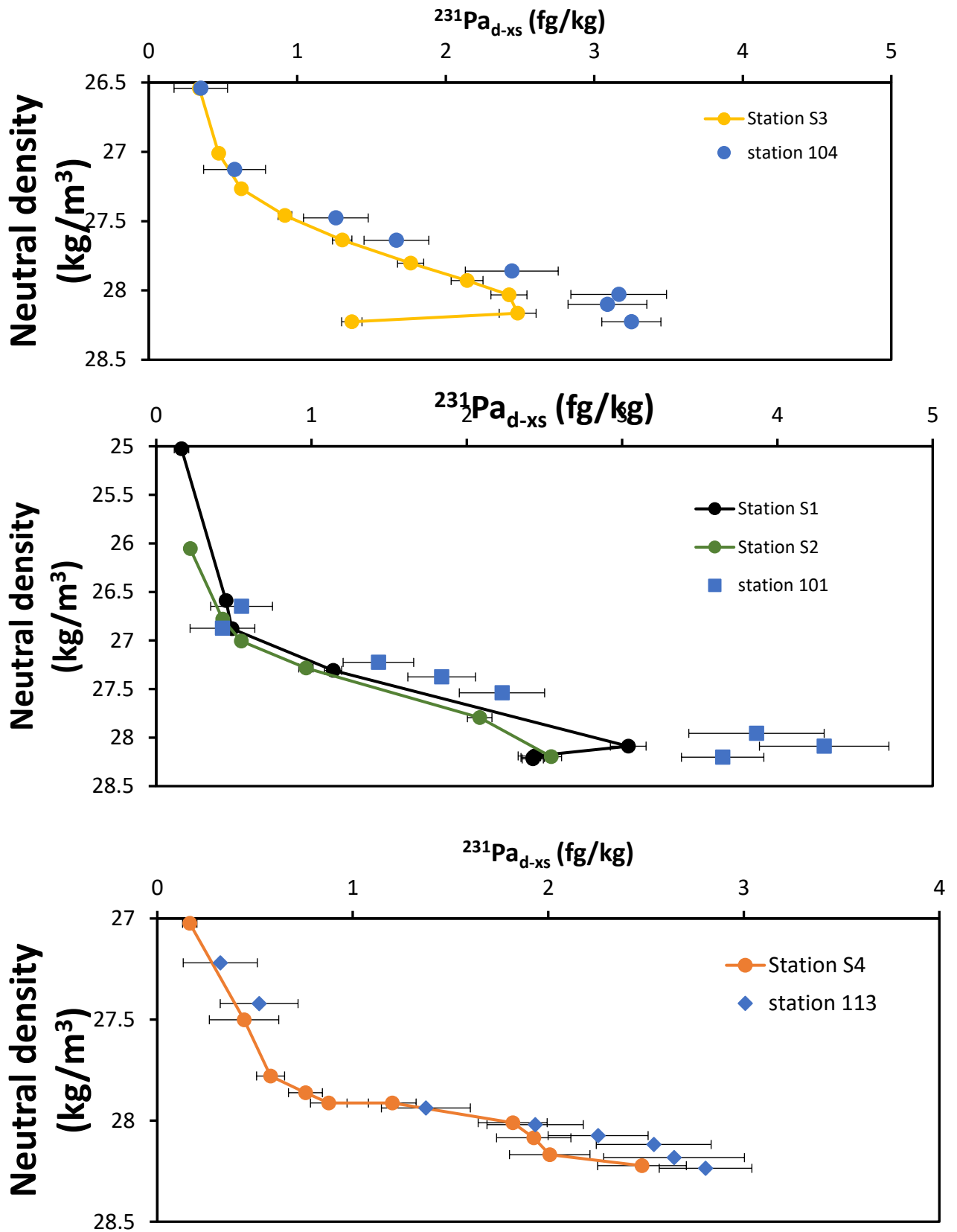


Figure ES10 : $^{231}\text{Pa}_{\text{d-xs-dissolved}}$ versus neutral during the Bonus GoodHope and ZeroDrake cruises at hydrologically close stations.

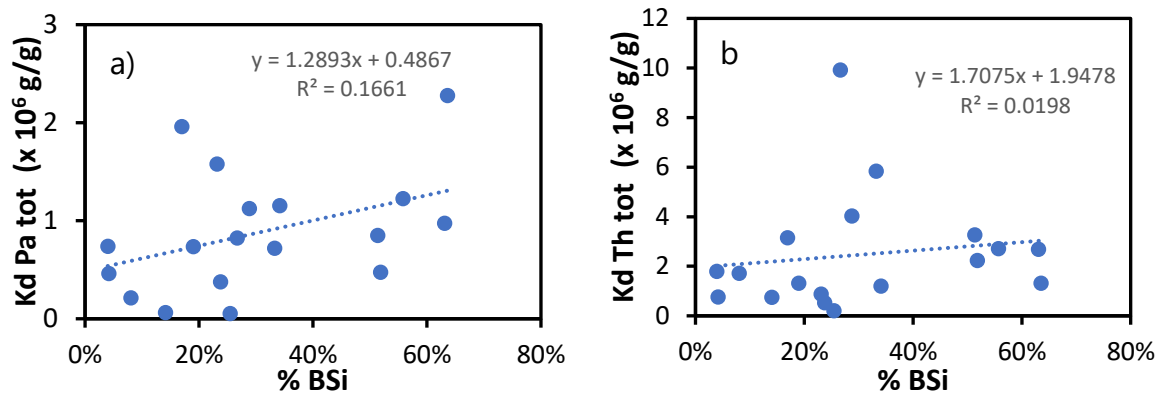


Figure ES2 : K_d estimated from the particulate and dissolved fraction, (a) for the ^{231}Pa and (b) for the ^{230}Th , against the estimated proportion of biogenic silica in the particulate fraction

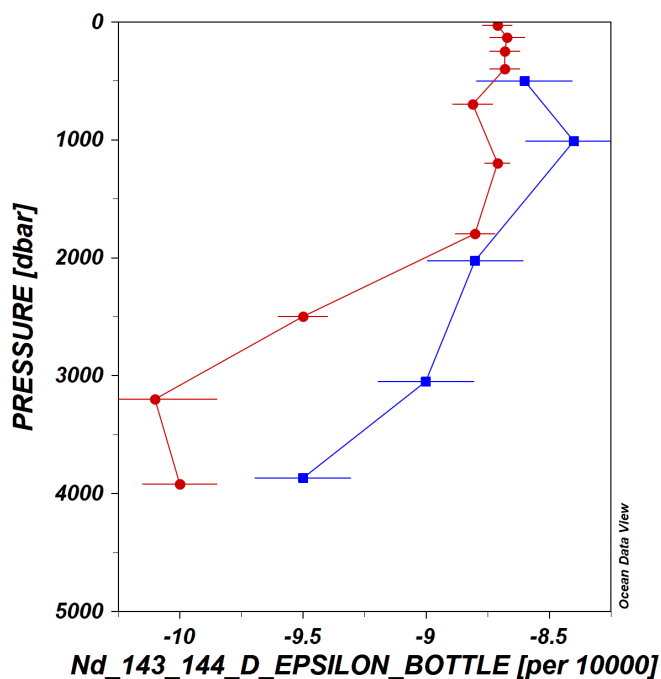


Figure ES3 : Comparison of epsilon Nd signature of BGH station S5 (red dot)(Garcia-Solsona et al. 2014) and the ZeroDrake station 131 (blue dot) (Stichel et al. 2012) compiled in the GEOTRACES intermediate report

Appendix 4 : Box model for ^{231}Pa fluxes:

We use a box to evaluate the weight of each ^{231}Pa transport flux relative to the *in situ* production. For each isopycnal surface, the box is bounded to the North and the south by the station corresponding to the end-members of the mixing (S1 and S4 for $\gamma_n = 27.865 \text{ kg/m}^3$; S3 and S5 for $\gamma_n = 28.094 \text{ kg/m}^3$). The horizontal length scale L is half of the distance between these end-member stations (Table 3-2). The mean height of the box is the depth of the isopycnal halfway to the 2 end-member stations. The width of the box used for an intermediate calculation, noted l , does not appear in the final result. We choose the mean dissolved and particulate of ^{231}Pa concentration of ^{231}Pa and ^{231}Pa at the depth of the isopycnal surface halfway between the 2 end-member stations. The *in situ* ^{231}Pa production rate in seawater is $P = 25 \text{ fg/m}^3/\text{y}$ using the output parameters from the advection-diffusion-scavenging model from Table ES1, we obtain:

$$\frac{F_{diff}}{F_{prod}} = \frac{l \times h \times \frac{^{231}\text{Pa}_d}{L} \times K_i}{P \times l \times h \times L} = \frac{K_i \times ^{231}\text{Pa}_d}{P \times L^2}$$

$$\frac{F_{adv}}{F_{prod}} = \frac{l \times h \times u_i \times ^{231}\text{Pa}_d}{P \times l \times h \times L} = \frac{^{231}\text{Pa}_d \times u_i}{P \times L}$$

$$\frac{F_{scav}}{F_{prod}} = \frac{l \times L \times w_p \times ^{231}\text{Pa}_p}{P \times l \times h \times L} = \frac{w_p \times ^{231}\text{Pa}_p}{h \times P}$$

$\frac{F_{diff}}{F_{prod}}$, $\frac{F_{adv}}{F_{prod}}$ and $\frac{F_{scav}}{F_{prod}}$ are given in Tab.

Table ES1 : Box-model parameters used and results

	$\gamma_n = 27.865 \text{ kg/m}^3$	$\gamma_n = 28.094 \text{ kg/m}^3$
L (m)	800000	500000
h (m)	1429	1205
P (fg/m ³ /y)	25	25
u_i (m/s)	0.0030	0.0031
K_i (m ² /s)	1900	1900
w_p (m/y)	990	340
$^{231}\text{Pa}_d$ (fg/m ³)	2000	2100
$^{231}\text{Pa}_p$ (fg/m ³)	15	18
$\frac{F_{adv}}{F_{prod}}$	946%	1642%
$\frac{F_{diff}}{F_{prod}}$	749%	2013%
$\frac{F_{scav}}{F_{prod}}$	41%	20%

Table ES2 : Dissolved concentration of ^{231}Pa from samples of the Bonus GoodHope cruise

Station	Depth (m)	θ ($^{\circ}\text{C}$)	Salinity	γ^n (kg/m^3)	$^{231}\text{Pa}_d$ (fg/kg)	$^{231}\text{Pa}_{d-x_s}$ (fg/kg)	DSi ($\mu\text{g/kg}$)	O_2 ($\mu\text{mol/kg}$)	Water mass
<i>Station S1: 36.50°S, 13.10°E, 4923 m bottom depth</i>									
	29	20.785	35.617	25.0222	0.19 ± 0.03	0.19 ± 0.03	2	233	ICW
	198	12.364	35.014	26.53	0.50 ± 0.02	0.50 ± 0.02	3.07	223	ICW
	397	9.824	34.757	26.7918	0.58 ± 0.02	0.58 ± 0.02	6.55	230	ICW
	753	4.973	34.346	27.1602	1.25 ± 0.03	1.25 ± 0.03	27	198	i-AAIW
	3005	1.945	34.836	27.8444	3.34 ± 0.06	3.34 ± 0.06	63	227	SE-NADW
	3981	0.892	34.749	27.8506	2.79 ± 0.06	2.78 ± 0.06	134	218	AABW
	4565	0.716	34.733	27.8493	2.86 ± 0.04	2.85 ± 0.04	126.95	217	AABW
	4907	0.568	34.72	27.8481	3.16 ± 0.04	3.15 ± 0.04	127.2	219	AABW
<i>Station S2: 42.47°S, 08.93°E, 4070 m bottom depth</i>									
	20	12.951	34.521	26.0547	0.23 ± 0.01	0.23 ± 0.01	0.22	272	ICW
	124	9.083	34.482	26.7815	0.46 ± 0.02	0.46 ± 0.02	2.5	262	ICW
	292	6.654	34.267	27.0053	0.61 ± 0.02	0.61 ± 0.02	9.27	273	ICW/a-AAIW
	595	4.138	34.185	27.2829	1.07 ± 0.03	1.07 ± 0.03	18.56	254	a-AAIW
	1453	2.626	34.585	27.7945	2.27 ± 0.04	2.26 ± 0.04	61.2	181	UCDW
	4021	0.81	34.741	28.1961	2.90 ± 0.04	2.90 ± 0.04	109	219	AABW
<i>Station S3: 47.55°S, 04.37°E, 4480 m bottom depth</i>									
	40	6.32	33.733	26.5685	0.36 ± 0.03	0.36 ± 0.03	0.52	303	AASW
	124	4.029	33.867	27.0072	0.51 ± 0.03	0.51 ± 0.03	7.2	306	AASW
	248	3.633	34.101	27.2697	0.69 ± 0.03	0.69 ± 0.03	15	272	AASW/a-AAIW
	495	2.739	34.233	27.4888	1.02 ± 0.03	1.02 ± 0.03	30	229	a-AAIW
	742	2.591	34.407	27.6574	1.43 ± 0.03	1.43 ± 0.03	55	189	a-AAIW/UCDW
	1068	2.447	34.575	27.8099	1.93 ± 0.04	1.93 ± 0.04	70.5	175	A_UCDW
	1482	2.334	34.716	27.936	2.36 ± 0.06	2.36 ± 0.06	72.9	186	SW-NADW
	2003	1.971	34.771	28.0376	2.68 ± 0.07	2.68 ± 0.07	80.38	203	SW-NADW
	3052	0.955	34.731	28.1653	2.75 ± 0.05	2.75 ± 0.05	99.84	210	SW-NADW
	4299	0.415	34.695	28.2262	1.67 ± 0.04	1.66 ± 0.04	120.1	213	AABW
<i>Station S4: 51.85°S, 00.00°E, 2570 m bottom depth</i>									
	59	2.521	33.712	27.0277	0.19 ± 0.02	0.19 ± 0.02	22.8	330	AASW
	168	0.827	34.033	27.4838	0.50 ± 0.10	0.50 ± 0.10	42.94	281	WW (AASW)
	248	1.543	34.433	27.7832	0.68 ± 0.04	0.68 ± 0.04	77.39	199	WW/DP-UCDW
	327	1.811	34.548	27.8553	0.89 ± 0.05	0.89 ± 0.05	-	178	DP-UCDW
	416	1.874	34.627	27.9165	1.05 ± 0.06	1.05 ± 0.06	83	175	DP-UCDW
	416	1.874	34.627	27.9165	1.36 ± 0.07	1.36 ± 0.07	83	175	DP-UCDW
	742	1.702	34.704	28.012	2.06 ± 0.10	2.06 ± 0.10	91.7	186	LCDW
	1117	1.42	34.727	28.08	2.23 ± 0.11	2.23 ± 0.11	100.99	199	LCDW
	1678	0.755	34.704	28.171	2.34 ± 0.12	2.34 ± 0.12	117	207	LCDW/AABW
	2307	0.359	34.689	28.225	2.84 ± 0.13	2.84 ± 0.13	127.19	212	AABW
<i>Intercal: 52.98°S, 00.00°E, 2624 m bottom depth</i>									
	380	1.81	34.63	27.929	1.54 ± 0.04	1.54 ± 0.04		179	UCDW
	500	1.78	34.68	27.979	1.79 ± 0.04	1.79 ± 0.04		183	LCDW
	1000	1.22	34.71	28.094	2.43 ± 0.05	2.43 ± 0.05		201	LCDW
<i>Station S5: 57.55°S, 00.03°W, 3932 m bottom depth</i>									
	30	0.40	34.078	27.559	0.71 ± 0.03	0.71 ± 0.03	68.9	344	WW(AASW)
	134	-0.671	34.355	27.8713	0.42 ± 0.04	0.42 ± 0.04	81.92	292	WW'AASW)
	396	0.529	34.674	28.154	1.84 ± 0.03	1.84 ± 0.03	107.81	206	WDW
	692	0.422	34.685	28.202	1.90 ± 0.09	1.90 ± 0.09	113.73	201	WDW
	1185	0.154	34.677	28.2434	2.29 ± 0.01	2.29 ± 0.01	-	215	WDW/WSDW
	1776	-0.104	34.668	28.2872	2.39 ± 0.06	2.39 ± 0.06	132.22	225	WDW/WSDW
	2462	-0.346	34.66	28.332	2.12 ± 0.08	2.12 ± 0.08	123.67	235	WSDW
	3848	-0.632	34.65	28.385	3.45 ± 0.06	3.45 ± 0.06	-	248	WSDW/WSBW

Table ES3 : Particulate ^{231}Pa from Bonus GoodHope samples and the FTh/Pa measured from the particulate measurement and a linear interpolation over dissolved sample

Depth (m)	$^{231}\text{Pa}_p$ (fg/kg)		$^{232}\text{Th}_p$ (fg/kg)		$^{231}\text{Pa}_{p-xS}$ (fg/kg)		BSi ($\mu\text{g/kg}$)	FTh/Pa	
<i>Station S1</i>									
30	0.006	± 0.001	7.0	± 0.1	0.005	± 0.001	18.82	2.41	± 0.55
199	0.005	± 0.001	18.8	± 0.3	0.004	± 0.001		10.53	± 1.76
1242	0.017	± 0.003	32.3	± 0.7	0.016	± 0.003		26.55	± 4.19
2687	0.020	± 0.003	37.8	± 0.5	0.018	± 0.003		15.52	± 2.48
2732	0.015	± 0.002	17.3	± 0.5	0.015	± 0.002		27.41	± 7.89
4628	0.341	± 0.054	371	± 10	0.325	± 0.052		10.60	± 1.74
<i>Station S2</i>									
20	0.017	± 0.004	4.1	± 0.1	0.016	± 0.004	2.7	2.95	± 0.7
257	0.007	± 0.003	8.9	± 0.1	0.007	± 0.003		13.10	± 5.99
601	0.007	± 0.002	5.4	± 0.1	0.007	± 0.002		14.61	± 4.11
1426	0.010	± 0.004	9.1	± 0.1	0.010	± 0.004		37.63	± 16.25
1941	0.006	± 0.001	8.5	± 0.1	0.006	± 0.001		25.82	± 4.16
2859	0.014	± 0.002	8.9	± 0.1	0.013	± 0.002		23.07	± 5.24
3858	0.106	± 0.017	93.1	± 1.2	0.103	± 0.016		13.19	± 2.14
<i>Station S3</i>									
40	0.003	± 0.001	7.1	± 0.1	0.003	± 0.001	21.50	16.49	± 5.87
594	0.018	± 0.002	4.41	± 0.04	0.017	± 0.002	6.72	8.452	± 1.24
1058	0.020	± 0.003	5.1	± 0.1	0.020	± 0.003	3.36	12.41	± 1.72
1985	0.023	± 0.003	5.5	± 0.1	0.023	± 0.003		12.58	± 1.80
3025	0.027	± 0.004	8.0	± 0.1	0.026	± 0.004		12.53	± 2.11
4262	0.021	± 0.003	2.5	± 0.0	0.021	± 0.003		3.12	± 0.47
<i>Station S4</i>									
59	0.001	± 0.000	0.076	± 0.001	0.001	± 0.000	20.16	3.83	± 0.90
169	0.019	± 0.001	1.48	± 0.02	0.019	± 0.001	24.86	2.66	± 0.54
258	0.028	± 0.004	2.42	± 0.02	0.028	± 0.004	18.82	2.23	± 0.35
743	0.030	± 0.001	2.23	± 0.02	0.030	± 0.001	8.74	3.88	± 0.21
1119	0.019	± 0.000	2.82	± 0.03	0.019	± 0.000	9.41	4.67	± 0.26
1682	0.013	± 0.002	2.23	± 0.02	0.012	± 0.002	2.02	7.89	± 1.19
2273	0.082	± 0.011	6.07	± 0.06	0.082	± 0.011	7.39	3.63	± 0.52
2469	0.115	± 0.016	6.25	± 0.06	0.115	± 0.015			
<i>Station S5</i>									
30	0.027	± 0.004	2.23	± 0.01	0.027	± 0.004			
139	0.023	± 0.001	2.1	± 0.1	0.023	± 0.001	8.064	0.57	± 0.06
248	0.079	± 0.003	2.5	± 0.1	0.079	± 0.003	15.46	0.57	± 0.03
694	0.043	± 0.007	3.6	± 0.8	0.043	± 0.007	6.72	1.05	± 0.20
1784	0.031	± 0.003	4.0	± 0.4	0.031	± 0.003	3.36	1.81	± 0.20
2478	0.063	± 0.002	8.5	± 0.1	0.063	± 0.002	2.69	1.68	± 0.10
3172	0.089	± 0.003	11.6	± 0.2	0.089	± 0.003	2.69	1.58	± 0.08
3840	0.179	± 0.006	26.1	± 0.3	0.178	± 0.006		1.62	± 0.08

Table ES4 : Major phases in filtered particles and Th and Pa partition coefficients for the bulk particulate matter and Pa partition coefficient estimated for pure opal.

station	depth (m)	Bsi (µg/kg)	CaCO ₃ (µg/kg)	²³² Th (pg/kg)	POM (µg/kg)	SPM (µg/kg)	% Opal (g/g)	K _d -bulk(Pa) ×10 ⁶ (g/g)	K _d -bulk(Th) ×10 ⁶ (g/g)	K _d -opal(Pa)* ×10 ⁶ (g/g)
1	25	18,82	33	6.96	26.7	79.2	24 %	0.378	0,536	-
2	70	2,69	19	6.49	45.6	67.9	4 %	0.741	1,803	1.62
3	41	21,50	55,2	7.06	75.4	152.8	14 %	0.062	0,757	-
3	600	6,72	5,7	4.41	7.4	20.2	33 %	0.719	5,848	0.59
3	1068	3,36	4,3	5.07	4.4	12.6	27 %	0.826	9,920	0.81
4	60	20,16	19	0.07	40	79.2	25 %	0.054	0,212	-
4	170	24,86	2,4	1.39	12.0	39.4	63 %	0.975	2,692	1.16
4	260	18,82	6,3	2.37	8.4	33.8	56 %	1.225	2,721	1.60
4	749	8,74	2,5	2.21	5.6	17.0	51 %	0.851	3,274	0.96
4	1128	9,41	2,5	2.76	6.0	18.1	52 %	0.474	2,243	0.23
4	1695	2,02	17	2.14	5.8	25.0	8 %	0.214	1,726	-
4	2305	7,39	12	6.06	5.7	25.7	29 %	1.125	4,029	1.80
5	140	8,06	6,4	2.09	20.2	34.9	23 %	1.578	0,881	4.55
5	250	15,46	2,1	2.42	6.5	24.3	64 %	2.279	1,315	3.17
5	700	6,72	3,1	3.48	9.5	19.7	34 %	1.153	1,199	2.00
5	1800	3,36	12,1	3.93	1.8	17.7	19 %	0.737	1,324	0.04
5	2500	2,69	58	8.31	3.0	64.5	4 %	0.460	0,768	-
5	3200	2,69	7	11.03	5.1	15.9	17 %	1.962	3,151	7.15

BSi from Fripiat and al. 2011, POM estimated from the POC (Cavagna et al., 2013) and ²³²Th from Roy-Barman and al. 2019

* The K_d-opal(²³¹Pa) reported here are only ones with the opal contribution to the total partition is significant toward the other phases of the particulate matter